Full-frequency correction of spatial impulse response in back-projection scheme using space-variant filtering for optoacoustic mesoscopy

Tong Lu[a,1], Yihan Wang[c,1], Jiao Li[a,b,*], Jaya Prakash[d], Feng Gao[a,b], Vasilis Ntziachristos[e]

[a] *College of Precision Instrument and Optoelectronics Engineering, Tianjin University, Tianjin, 300072, China*
[b] *Tianjin Key Laboratory of Biomedical Detecting Techniques and Instruments, Tianjin, 300072, China*
[c] *School of Life Science and Technology, Xidian University, Xi'an, 710071, China*
[d] *Department of Instrumentation and Applied Physics, Indian Institute of Science, Bangaluru, 60012, India*
[e] *Institute for Biological and Medical Imaging, Technical University of Munich and Helmholtz Center Munich, Neuherberg, 85764, Germany*

ARTICLE INFO

ABSTRACT

The fidelity and quality of reconstructed images in optoacoustic mesoscopy (OPAM) can be significantly improved by considering the spatial impulse response (SIR) of the employed focused transducer into reconstruction. However, the traditional method fully taking the SIR into account can hardly meet the data-intensive requirements of high resolution OPAM because of excessive memory and time consumption. Herein, a modified back-projection method using a space-variant filter for full-frequency correction of the SIR is presented, and applied to the OPAM system with a sphere-focused transducer. The proposed method can readily manage the large datasets of the OPAM and effectively reduce the extra time consumption. The performance of the proposed method is showcased by simulations and experiments of phantoms and biological tissue. The results demonstrate that the modified back-projection method exhibits better image fidelity, resolution and contrast compared to the common and weighted back-projection methods that are not or not fully accounting for the SIR.

1. Introduction

Optoacoustic microscopy can be implemented in two approaches, i.e. optical resolution optoacoustic microscopy (OR-OAM) and acoustic resolution optoacoustic microscopy (AR-OAM). OR-OAM can provide optical images where in the imaging resolution is limited by light focusing, while AR-OAM (also known as optoacoustic mesoscopy (OPAM)) has the ability to provide optical images at acoustic resolution operating at greater imaging depths [1–6]. OPAM pushes the imaging depths to 10 mm at an imaging resolution of $4-100$ μm using a high-frequency focused ultrasound transducer having $10-100$ MHz frequency range [7–9]. OPAM bridges the gap between microscopic and macroscopic imaging, making OPAM attractive for understanding the biological mechanisms [7,8], tissue pathophysiology [9,10] and dermatological applications [11,12]. Many reconstruction algorithms based on time-reversal, delay and sum, spherical radon transform, and model-based method have been developed to reconstruct optoacoustic images with improved image quality [13–22]. Further modeling transducer characteristics, such as the impulse response is known to impact the image quality, especially for the piezoelectric transducer

[23,24].

OPAM utilizes transducers with high center frequency to capture high-frequency signals generated by small-size objects, and a focused transducer with the high numerical aperture (NA) is commonly employed to increase the detection sensitivity of the generated high-frequency signals. The recorded optoacoustic signal using piezoelectric transducers is a convolution of the original optoacoustic signal with the electrical impulse response (EIR) and the spatial impulse response (SIR) of the transducer [23]. EIR depends on the electrical property of the piezoelectric crystal and is defined as a band-pass filter around the center frequency of the transducer. The SIR, determined by the shape of the transducer, is a spatially-dependent low-pass filter affecting the amplitude and frequency of the signals [23–25]. Previous works have shown that modeling impulse response of the transducer in the optoacoustic reconstruction process can provide better image quality and image fidelity [23–27]. However, there is still not a precise and fast way to fully consider the SIR for the high-resolution OPAM.

Image deconvolution approaches have been developed to improve the reconstructed optoacoustic images [22,28,29]. However these approaches do not model transducer characteristics, further algorithms

---

have been proposed to remove the influence of EIR by deconvolving the recorded optoacoustic signals with the EIR of the transducer [25,30,31] and many groups have also modeled SIR in the optoacoustic reconstruction process [23–27,32–35]. SIR has been successfully incorporated into the forward model while performing model-based optoacoustic inversions [26,27]. In Ref [27], the finite-sized transducer was discretized into smaller elements and with an assumption of the SIR of all these smaller elements to be the same, the resultant transducer SIR was modeled as a super-position of the SIR of these smaller elements. Only model-based algorithms have been reported to fully consider the influence of SIR on the signal's amplitude and frequency in the optoacoustic reconstruction [27]. However, model-based schemes are associated with huge memory requirements, and high computational complexity/load [13,14,27], and these works have modeled transducer properties for larger sample size and with low frequency transducers (having center frequency of $2.5 - 5$ MHz). Note that the acceleration of reconstruction process and the reduction of the computational load have been realized on graphics processing unit (GPU) [26], however modeling the transducer characteristics within the model-based scheme is still thousand times slower than common back-projection (CBP) algorithms. Therefore, time domain (direct back-projection formula) algorithms are commonly used in OPAM for fast and efficient computation, while considering the massive size of the acquired optoacoustic data and the finer mesh grids of reconstructed optoacoustic images required for generating high quality OPAM images. Prior works have focused on modeling the SIR through weighted back-projection (WBP) algorithms [25,32–34]. A commonly used approach for modeling SIR, is to take the maximum values of SIR at different locations for building a weight matrix, this weight matrix provides a spatially-varying amplitude for the back-projection algorithm. Most of the prior works have just considered the spatially varying response of the SIR, but ignored the frequency dependent impact of the SIR modeling [32–34]. A frequency-dependent approach has been presented to decrease the signal distortion in both magnitude and bandwidth caused by the SIR, through obtaining the summation of the reconstructed results using weighted matrices at several selected frequencies [25]. However, for the broadband optoacoustic signals, the computation of weighted matrixes to cover the whole bandwidth of signals is computationally expensive. In Ref. [35], a spatiotemporal optimal filter is designed to compensate for the SIR in the mean square error sense, and the image resolution is significantly improved by the model-based correction method which is actually a back-projection method. However, this method is not suitable for OPAM with large datasets, because of the huge matrix construction and inversion during the calculation of the filter matrix.

In order to find an efficient way to accurately account for the SIR in high-resolution OPAM, we present a new method to fully integrate the effect of SIR using a space-variant filter in the back-projection algorithm. At different spatial positions, the space-variant filter corresponding to the SIR of the employed transducer is constructed to deconvolve the distorted signal. The SIR can be obtained from an analytical solution [36,37] and several toolboxes [38,39]. The parallel version of the proposed method was also implemented on GPU to accelerate the reconstruction process close to the CBP algorithm. The performance of the proposed method is compared with the CBP and WBP methods in both simulation results and experiment results of phantoms and *ex vivo* biological tissue.

2. Method and material

2.1. Background

A common back-projection algorithm can be written as follows [18]:

$$p_0(\mathbf{r}) = \frac{1}{\Omega_0} \int_s d\Omega \left[2p(\mathbf{r}', t) - 2t \frac{\partial p(\mathbf{r}', t)}{\partial t} \right] \Bigg|_{t = |\mathbf{r}' - \mathbf{r}|/c}, \tag{1}$$

where $d\Omega$ is the solid angle element and Ω_0 is the solid angle related to the whole transducer surface S, t is the time, and c is the speed of sound in the medium. $p(\mathbf{r}', t)$ is the signal received at different detecting position $\mathbf{r}'$, $p_0(\mathbf{r})$ is the distribution of initial optoacoustic pressure p_0 at reconstruction position $\mathbf{r}$. In the practical OPAM systems, the piezoelectric transducer with a finite size is usually employed, which means the optoacoustic signal suffers the distortion by the influence of EIR and SIR. First, the effect of EIR can be removed using previously developed approach described in Ref [24]. The derivative of the EIR can be obtained by measuring the optoacoustic signal generated by a point-like absorber located at the focus of transducer. Then, the derivative of the measured signals is deconvolved with the derivative of the EIR. Here, for convenience, we define $b(\mathbf{r}', t)$ as the back-projection term, $p_s(\mathbf{r}', t)$ as the deconvolution results of the back-projection term $b(\mathbf{r}', t)$, which can be expressed as:

$$p_s(t) = deconv(\text{EIR}, b(\mathbf{r}', t)) \tag{2}$$

where *deconv* means the deconvolution process. As the influence of EIR has been removed, a discrete and simplified version of Eq. (1) can be expressed as:

$$p_0(\mathbf{r}_m) = \sum_k p_s(\mathbf{r}'_k, t_{km}), \tag{3}$$

where $\mathbf{r}'_k$ is the detection position of the kth measuring point, $\mathbf{r}_m$ is the reconstruction position of the mth point of the region of interest (ROI), and $t_{km} = |\mathbf{r}'_k - \mathbf{r}_m|/c$.

2.2. Construction of space-variant filter

When the optoacoustic signal generated from a specific spatial location is detected by an ultrasound transducer with a finite surface S, the optoacoustic signal will arrived at the different points $\mathbf{r}_d$ on the transducer surface at different times. Thus, the SIR can be mathematically expressed as the integral of the optoacoustic field obtained by the transducer surface:

$$h_s(\mathbf{r}, t) = \int_s \frac{\delta\left(t - \frac{|\mathbf{r}_d - \mathbf{r}|}{c}\right)}{|\mathbf{r}_d - \mathbf{r}|} d\mathbf{r}_d, \tag{4}$$

where $h_s(\mathbf{r}, t)$ is the SIR. By setting the parameters such as the ROI, the sampling frequency and the shape of transducer, the corresponding solution of SIRs in the ROI can be obtained. The exact analytical solution of SIR for different shapes, such as rectangular transducer [36] and slightly sphere-focused transducer [37], have been analytically derived. Furthermore, the simulation toolboxes Field II [38] and DREAM [39] can also calculate the specified SIR which are almost the same with the exact analytical solution. The constructed spatial-variant filter $h^k(\mathbf{r}, t)$ is the SIR vector $h_s(\mathbf{r}, t)$ at the kth measuring point. We calculate a space-variant filter consisting of a specific SIR calculated at a specific spatial position according to the detection position. All the space-variant filters at different spatial positions according to the detection position can be combined into a matrix form.

2.3. Space-variant filter in back-projection scheme

The space-variant filter $h^k(\mathbf{r}, t)$ is designed to compensate for the SIR in the direct back-projection algorithm. At a single projection angle of θ, the SIR filter can be considered as $h^k(d, t)$, changing with the propagated distances. Since the distance corresponds to the propagation time, the SIR filter can also be regarded as an output changed with two-dimension time, of which expression is equivalent to the time-variant filter established to correct the acoustic attenuation [40]. A particular form of non-stationary convolution usually applied in

seismology [41] can be used to formulate the time-variant filtering method. It can be mathematically expressed as:

$$p_0(t) = \sum_{\tau} h(t, t - \tau) p_s(\tau),$$

(5)

where $h(t, t - \tau)$ is the time-variant filter varying as a function of output time. We expand this definition for the space-variant filter in the back-projection scheme which can be expressed mathematically as:

$$p_0^k(\mathbf{r}) = p_{0,\mathbf{r}}^k(t) = \sum_{\tau} h_{\mathbf{r}}^k(t, t - \tau) p_s^k(\tau),$$

(6)

where $\mathbf{r} = [ct\cos\theta, ct\sin\theta]$. One position corresponds to one time point, so the space-variant filter $h^k(\mathbf{r}, t)$ can be rewritten as $h_{\mathbf{r}}^k(t, t - \tau)$. The general back-projection reconstruction algorithm can be easily understood as projecting the measured signals to different spatial positions, which is equal to perform the convolution with the impulse functions ($\delta(t - d/c)$). The SIRBP method proposed in this paper employs spatial-variant filters to replace the impulse functions, realizing the convolution with the measured signal received at the detection position. In Eq. (6), the optoacoustic signal $p_s^k(\tau)$ is received by the employed transducer at kth detection point. A space-variant filter consisting of a specific SIR can be calculated at a specific spatial position with respect to the detection position in the ROI. The space-variant filters $h_{\mathbf{r}}^k(t, t - \tau)$ at different spatial positions with respect to the detection position in the ROI can be constructed into a matrix form. Then the image of $p_0^k(\mathbf{r})$ at the kth detection point can be reconstructed. In practice, a matrix form of Eq. (6) can be expressed as:

$$\begin{bmatrix} p_0^k(\mathbf{r}_1) \\ \vdots \\ p_0^k(\mathbf{r}_M) \end{bmatrix} = \begin{bmatrix} h_{\mathbf{r}_1}^k(t_1, t_1 - \tau_1) & \cdots & h_{\mathbf{r}_1}^k(t_1, t_1 - \tau_N) \\ \vdots & & \vdots \\ h_{\mathbf{r}_M}^k(t_M, t_M - \tau_1) & \cdots & h_{\mathbf{r}_M}^k(t_M, t_M - \tau_N) \end{bmatrix} \begin{bmatrix} p_s^k(\tau_1) \\ \vdots \\ p_s^k(\tau_N) \end{bmatrix}.$$

(7)

The size of the matrix $\mathbf{h}_{\mathbf{r}}^k$ is $M \times N$, where M is the total number of reconstruction positions (equal to the number of space-variant filters), N is the time length of the detected optoacoustic signal (equal to the size of space-variant filter). Since each row of the matrix in Eq. (7) is independent, the matrix can be split into lots of vectors to allow parallel computation by GPU framework. The final image of initial optoacoustic pressure p_0 can be obtained by the summation of all the images of $p_0^k(\mathbf{r})$ from all the detection positions. As the space-variant filters depend on the relative positions between the reconstruction positions and the detection position, the filter matrix do not need recalculation at different detection positions or in different scanning geometries.

Fig. 1 shows the filtering process on the optoacoustic signal $p_s^k(t)$ received at kth detection point. Two specified positions with the same distance d are selected, that is to say $|\mathbf{r}_i| = |\mathbf{r}_j| = d = ct_n$. It can be observed that even at the same time t_n, the space-variant filters at two different spatial positions are different. This situation arises because the spherical wave propagating from two different spatial locations could be detected by the detector surface with different phase. The influence of SIR on the amplitude and frequency of the signal can be clearly understood from Fig. 1.

2.4. Experimental setup

The OPAM system used to evaluate the performance of the proposed method with experiment data was shown in Fig. 2. A tunable optical parametric oscillator laser (Opotek Inc., Carlsbad, CA, USA) provided the short-pulsed laser light with a repetition rate of 10 Hz and sub-10 ns pulse duration. The illumination light at the wavelength of 700 nm was guided into a custom-made 640-fiber bundle, then partitioned into four arms. A sphere-focused ultrasound transducer with the center frequency of 15 MHz, the focal length of 19.8 mm and the diameter of 6 mm was mounted on two motorized precision stages: a translation stage and a rotation stage (M-605.2DD and M-062.PD, Physik Instrumente, GmbH, Germany). The stages were selected to implement a translate-rotate scanning described in detail elsewhere [42]. The optoacoustic
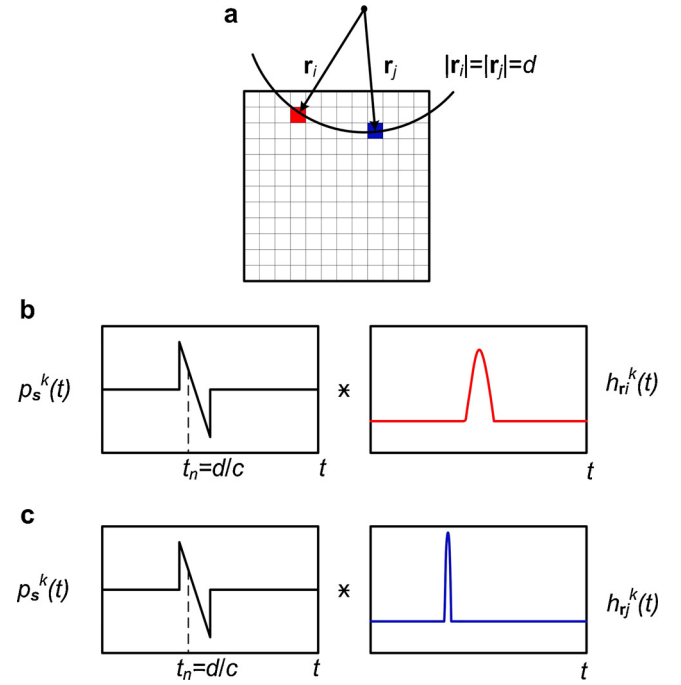

Fig. 1. The filtering process on the optoacoustic signal $p_s^k(t)$ by the proposed space-variant filter method. (a) Two different spatial positions have the same distance d from the transducer surface. (b) At position $\mathbf{r}_i$, the space-variant filter $h_{\mathbf{r}i}^k(t)$ is acted on the optoacoustic signal, which is different from the space-variant filter $h_{\mathbf{r}j}^k(t)$ in (c) at the position $\mathbf{r}_j$.

signals were first amplified by a 50 dB amplifier, then were digitized via a data acquisition (DAQ) card with a sampling rate of 125 MS/s, and finally were stored by the computer controlling system. The scanning radius of transducer was set to be 20 mm, approximately equal to the focal length. The transducer, the heads of the four-arm fiber and the samples were immersed in water for the acoustic coupling. The water temperature was maintained at 20℃, corresponding to the speed of sound of 1480 m/s.

2.5. Numerical and experimental samples

1) Simulation study: A phantom including absorbers of 60 μm, 100 μm, 120 μm and 200 μm diameter was used to quantitatively access the imaging performance of the proposed method for OPAM. To reduce the acquisition time, a sphere-focused transducer with focal length of 10 mm and diameter of 3.4 mm was employed, scaled down in equal proportion according to the transducer used in practice. The focal point was coincident with the center of the phantom. 3600 detecting positions covered an angle of 360° with a 2 deg angular step, and linearly moved in the range of 10 mm with a step of 500 μm. The ROI of 7 mm × 7 mm was discretized into 350 pixel × 350 pixel. The simulated optoacoustic signals were generated by a simulation toolbox of K-Wave [43]. In order to test the robustness of the proposed method, a white Gaussian noise was further added to the simulated data with the signal-to-noise ratio (SNR) of 15 dB.

2) *Sample 1: Absorbing microspheres with the diameter of 50 μm:* To test the enhancement of the spatial resolution by the proposed method, a group of microspheres were randomly dispersed in agar gel and molded to a cylinder with the diameter of 12 mm. 4320 detecting positions covered an angle of 360° with a 2 deg angular step, and linearly moved in the range of 12 mm with a step of 500 μm.

3) *Sample 2: Absorbing microspheres with the diameter of 100 μm:* To verify the image quality of the reconstructed image obtained by the proposed method, microspheres with bigger diameter were chosen to form the sample 2. 3600 detecting positions covered an angle of
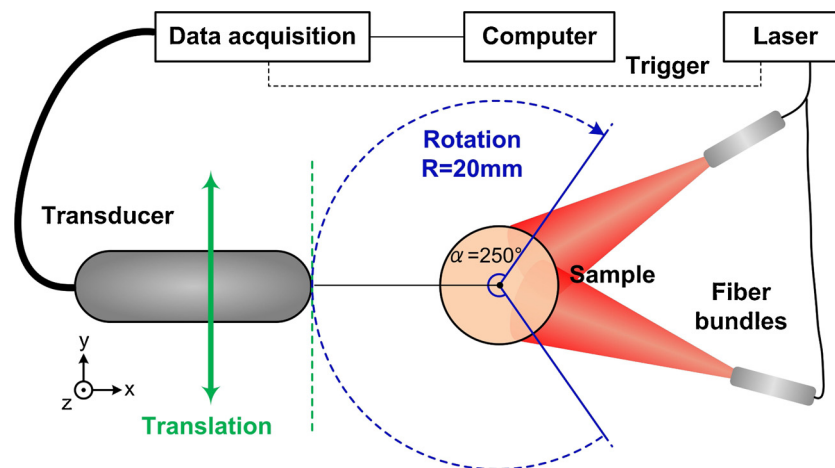
Fig. 2. Schematic top view of the set-up and scan geometry.

360° with a 2 deg angular step, and linearly moved in the range of 12 mm with a step of 600 μm.

4) *Sample 3: Mouse kidney:* To evaluate the performance of the proposed method in real biological tissues, the *ex vivo* mouse kidney was imaged. The sample was chosen for its abundant vessel branches with various sizes. The settings of detecting positions were consistent with those in sample 2.

2.6. Image reconstruction methods

In the numerical simulation, the EIR of the transducer are not provided thus the recorded data are only influenced by the SIR of the virtual transducer. The reconstructed results of the proposed method (abbreviated as the SIRBP method in the following) were compared with several reconstructed images performed by the CBP method, the WBP method with the weighted matrix consisting of the maximum value of SIR (WBPS) and the weighted matrix composed by the sensitivity field of some single-frequency signals. The WBP methods with the weighted matrix composed by the sensitivity field of the signal of 5 MHz, 15 MHz and 25 MHz were named as WBP5, WBP15 and WBP25 methods, respectively. The pixel size of reconstructed images was set to be 10 μm. In the experiments, the WBPS method usually adopted in the optoacoustic reconstruction procedure was selected among the WBP methods to comparison. All the reconstructed methods were conducted on the identical data. A band-pass filter from 0.1 MHz to 28 MHz (Butterworth, order 3) was employed for noise removal before reconstruction. The pixel size of reconstructed images was set to be 10 μm. The derivative of EIR of the used transducer was obtained by measuring the signal generated by a point-like microsphere with the diameter of 20 μm. The image results were initially reconstructed by CBP method. Subsequently, the measured optoacoustic signals were corrected with the experimentally derivative of EIR and then used to reconstruct the EIRBP results. The WBPS and SIRBP results were both reconstructed by the measured signals already deconvolved with the EIR. The exact analytical solution of the SIR of the employed transducer was calculated [37] and then used in the SIRBP method. The measured signals from different detecting positions can be simultaneously reconstructed by multiple threads, and a loop was added in each thread for the time length of the SIR in SIRBP method. All the mentioned reconstructed methods were executed on the GPU framework. The computational time in a GPU framework of the SIRBP method is about 15 times longer than the CBP method (when the run time of CBP method is 0.12 s, the SIRBP method needs 1.79 s for the same ROI). The computations were done on a NVIDIA GTX 750 GPU with 64 GB memory. In this work, with the pixel number of (350×350) and the time length of (1×1000), the size of the filter matrix is $(350 \times 350) \times (1 \times 1000)$

with sparse characteristics. No nonlinear processing method is applied in all the reconstructed images in this paper.

3. Results

3.1. Results from simulation data

Fig. 3 shows the original image and the reconstructed images obtained by six different algorithms after normalization. The cross-section profiles of the microspheres in Fig. 3 have been shown in Fig. S3. In Fig. 3b, the CBP result presents streak-type artifacts on the whole background, mainly resulting from the heterogeneous sensitivity field of the sphere-focused transducer. A series of WBP results and the SIRBP result have better performance in background noise suppression. The spider artifacts are clearly observed in the WBPS, WBP15 and WBP25 results, which are disappeared in the WBP5 result and the SIRBP result. The SIRBP result offers the darkest background and minimal artifacts.

In order to evaluate the reconstructed results of different algorithms explicitly, we calculate the contrast-to-noise ratio (CNR) and full width at half maximum (FWHM) of absorbers. Both the CNR and FWHM are the average of each three absorbers with the same size. Furthermore, a noisy simulation data (with the SNR of 15 dB) is adopted to evaluate the stability and robustness of the proposed algorithm. By considering the sensitivity heterogeneity of used transducer, the CNR values of last five results are all higher than the CBP result. In Fig. 4a, the CNR values of SIRBP image and WBP25 image are higher in all the absorbers of four different sizes in both noiseless and noisy situations. The CNR value of each size absorber in SIRBP image is around 25 dB higher than CBP image. There is a reasonable downward trend of CNR in all the reconstructed results compared with the noiseless results, expressed in Fig. 4a by the white lines. In the noisy situation, in addition to the almost similar CNR values of the 60 μm-diameter absorbers in the WBP25 and SIRBP results, the CNR values of the absorbers of other sizes in the SIRBP result are highest than all the other reconstructed results. Although in a noisy situation, the CNR value of each size absorber in SIRBP image is around 20 dB higher than CBP image.

In Fig. 4b, for the 60 μm-diameter absorbers, the FWHM value of WBP5 result is obviously deviated from the real size, while the FWHM of WBP25 result among the WBP results is smallest. On the other hand, for the 200 μm-diameter absorbers, the FWHM of WBP25 result is too small and the FWHM of WBP5 result is closest to the real size among the WBP results. The FWHM values of WBP15 result are similar to those of WBPS result, as the green line is almost overlapped with the brown line in Fig. 4b. For both the 60 μm-diameter and 200 μm-diameter absorbers, the FWHMs of SIRBP result are closest to the corresponding real size. Overall, the FWHM value of SIRBP results shown in the red line is
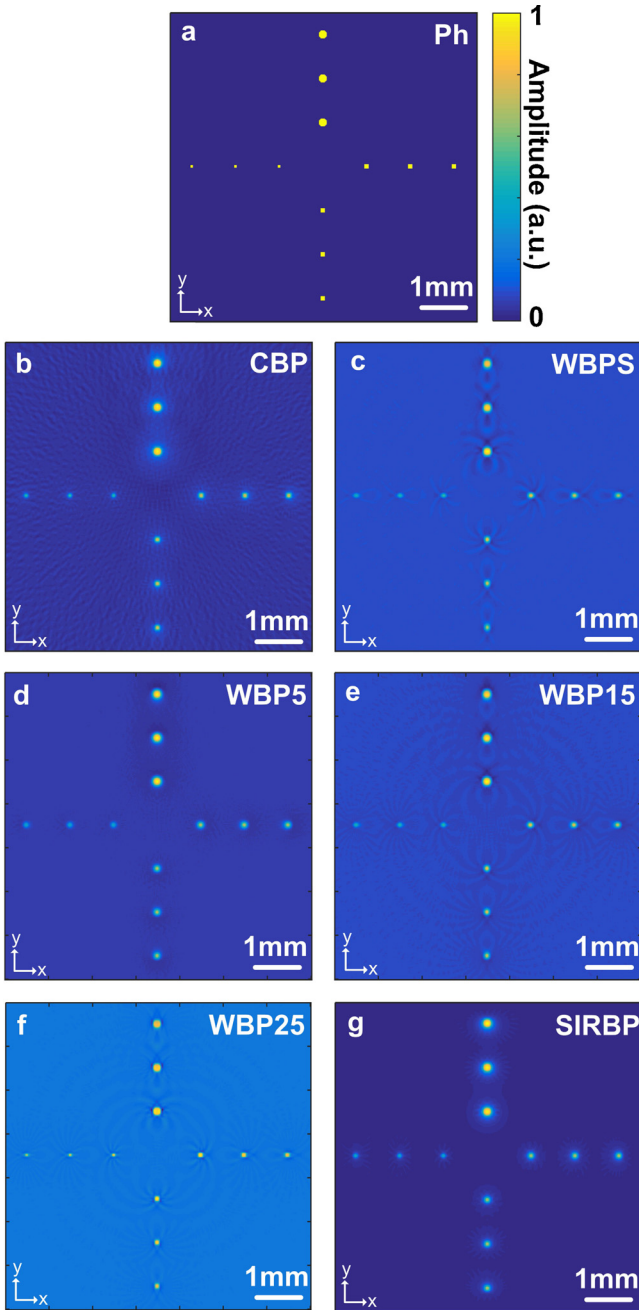
Fig. 3. (Simulation) The original image containing different sizes absorbers and the reconstructed images obtained by six different algorithms after normalization. (a) Numerical phantom (Ph). Reconstructions performed with (b) the CBP method, (c) the WBPS method, (d) the WBP5 method, (e) the WBP15 method, (f) the WBP25 method and (g) the SIRBP method. The diameters of absorbers are: 60 μm, 100 μm, 120 μm and 200 μm, respectively. Images are shown in the same colorbar after normalization.

closest to the standard black line.

To quantitatively assess the reconstruction by different reconstructed methods, the parameter d showing the difference between the reconstructed image and the original image is defined as

$$d = \sqrt{\left(\sum_{i=1}^{N_x}\sum_{j=1}^{N_y}(f_{i,j} - r_{i,j})^2\Big/\sum_{i=1}^{N_x}\sum_{j=1}^{N_y}r_{i,j}^2\right)}, \tag{8}$$

where f is the reconstructed image and r is the original image. The size of the image is $N_x \times N_y$. The smaller value of d indicates the better image fidelity of the reconstructed result compared to the original phantom
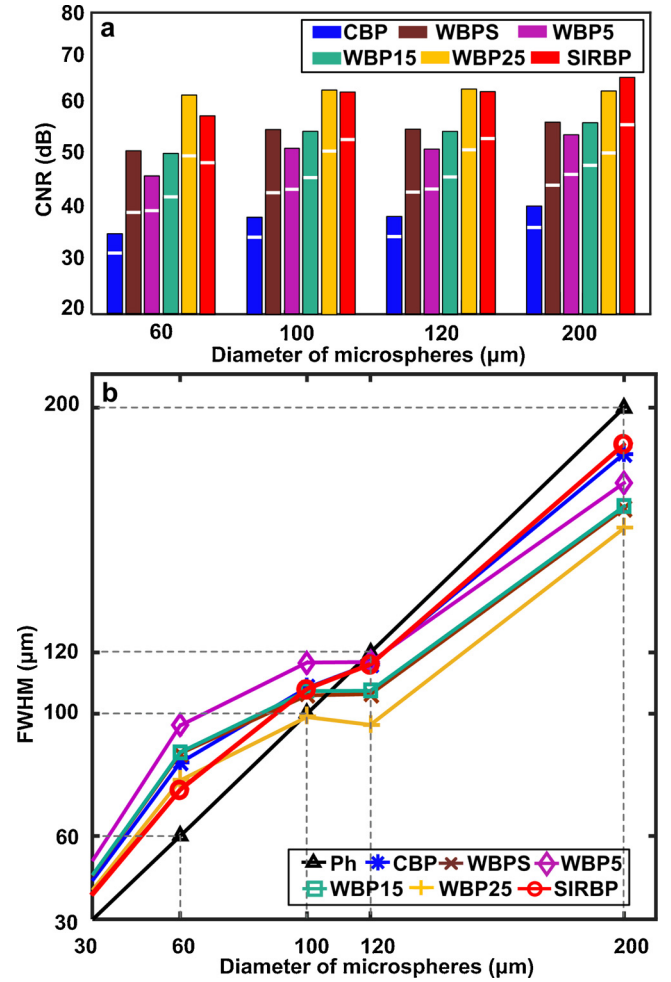

Fig. 4. (Simulation) Analysis parameters of the reconstructed images of four different sizes absorbers by six different methods. (a) CNR of the reconstructed images of four different sizes absorbers by six different methods. (b) FWHM of the reconstructed images of four different sizes absorbers by six different methods.

image. Furthermore, the universal quality index (*UQI*) representing the similarity between the reconstructed image and the original image is expressed as

$$UQI\{f, r\} = \frac{2\text{Cov}\{f, r\}}{(\sigma_f)^2 + (\sigma_r)^2}\frac{2\bar{f}\,\bar{r}}{(\bar{f})^2 + (\bar{r})^2}, \tag{9}$$

where $\bar{f}$ is the mean of reconstructed image, $\bar{r}$ is the mean of the original image, σ_f and σ_r are the variances of the reconstructed image and reference image, respectively. $\text{Cov}\{f, r\}$ is the covariance. The larger value of *UQI* suggests that the reconstructed image is more similar to the exact one. Besides, the peak signal-to-noise ratio (*PSNR*) of the reconstructed result is also calculated, which is defined as

$$PSNR = 10 \times \log_{10}\left(N_x N_y\Big/\sum_{i=1}^{N_x}\sum_{j=1}^{N_y}(f_{i,j} - r_{i,j})^2\right). \tag{10}$$

We calculated these three indexes for the six different reconstruction methods, and the numerical results are given in Table 1. Compared to the CBP result, the three indexes of the WBP results are all weakened while those of the SIRBP result is enhanced. The increase of the *PSNR* value and *UQI* value are 4.358 dB and 0.272, respectively. The d value is reduced by 0.339.

Table 1
PSNR, *d* and *UQI* of reconstructed results by different algorithms.

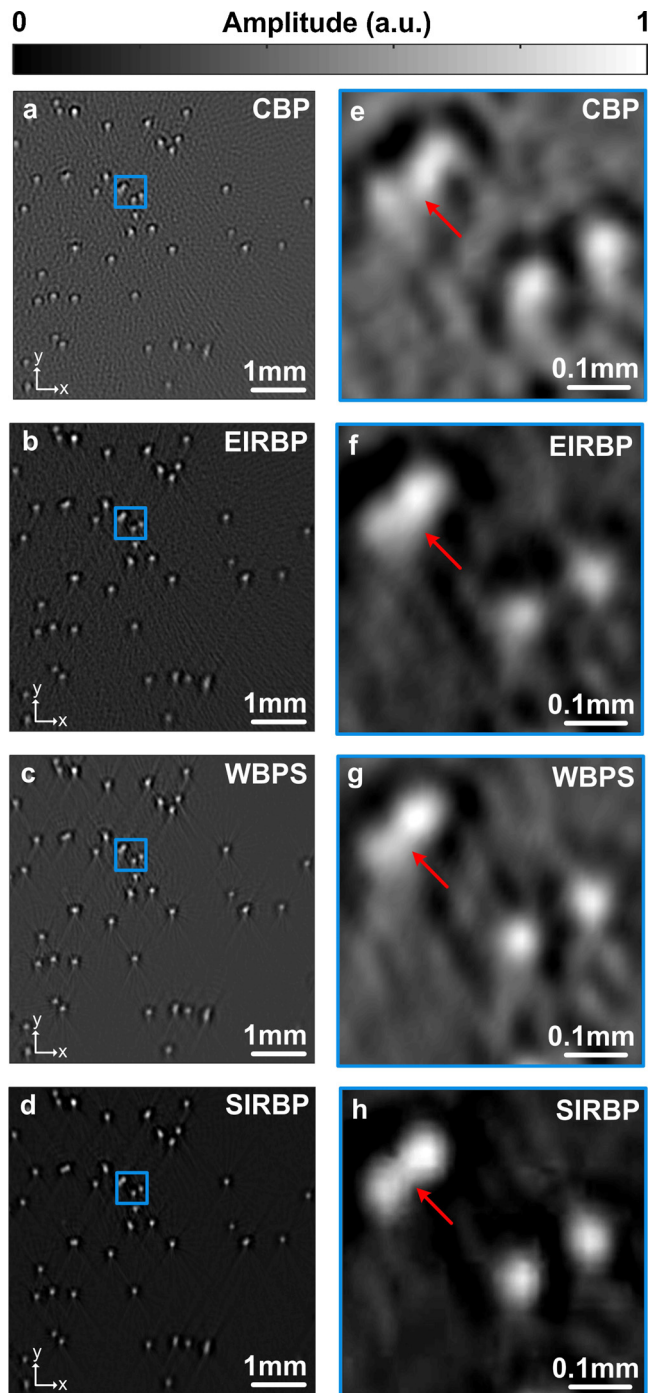|	CBP	WBPS	WBP5	WBP15	WBP25	SIRBP
PSNR (dB)	26.581	20.627	24.894	21.760	13.835	30.939
d	0.893	1.773	1.085	1.556	3.875	0.554
UQI	0.165	0.068	0.118	0.078	0.030	0.437

Fig. 5. (Experiment) Image reconstructions of 50 μm-diameter microspheres with (a) the CBP method, (b) the EIRBP method, (c) the WBPS method and (d) the SIRBP method. (e)-(h) are the zoom-in images of the blue square marked in the four methods. Images are shown in the same colorbar after normalization.

Fig. 6. (Experiment) Image reconstructions of 100 μm-diameter microspheres with (a) the CBP method, (b) the EIRBP method, (c) the WBPS method and (d) the SIRBP method. (e)-(h) are the zoom-in images of the blue square marked in the four methods. Images are shown in the same colorbar after normalization.
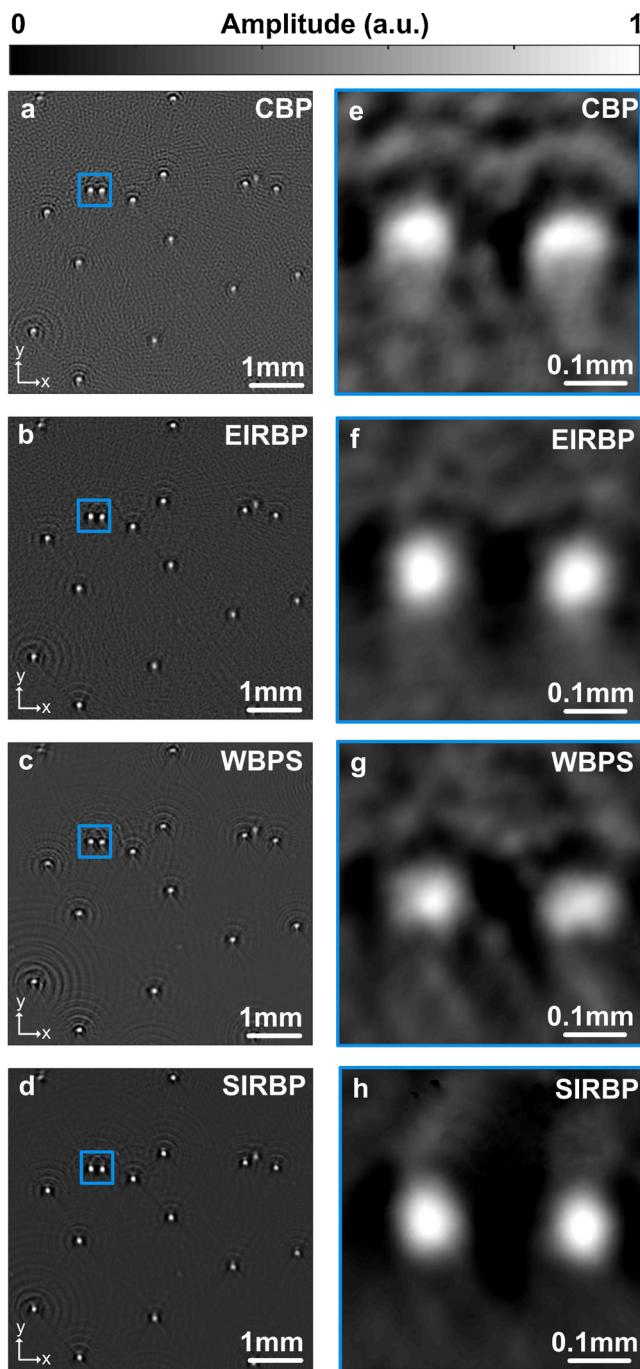
3.2. Results from experimental data

Fig. 5 shows the reconstructed results of 50 μm-diameter microspheres (sample 1) by use of the CBP, EIRBP, WBPS and SIRBP methods. When the influence of EIR is removed, the background of the EIRBP result (Fig. 5b) is obviously suppressed compared with the CBP result (Fig. 5a). With the maximum value of SIR as the weighted matrix in WBP algorithm, the homogeneity of background in Fig. 5c is enhanced but the magnitude of background is increased. The effective suppression on the background noise by the SIRBP method can be observed in Fig. 5d. The enlarged views of several randomly selected microspheres
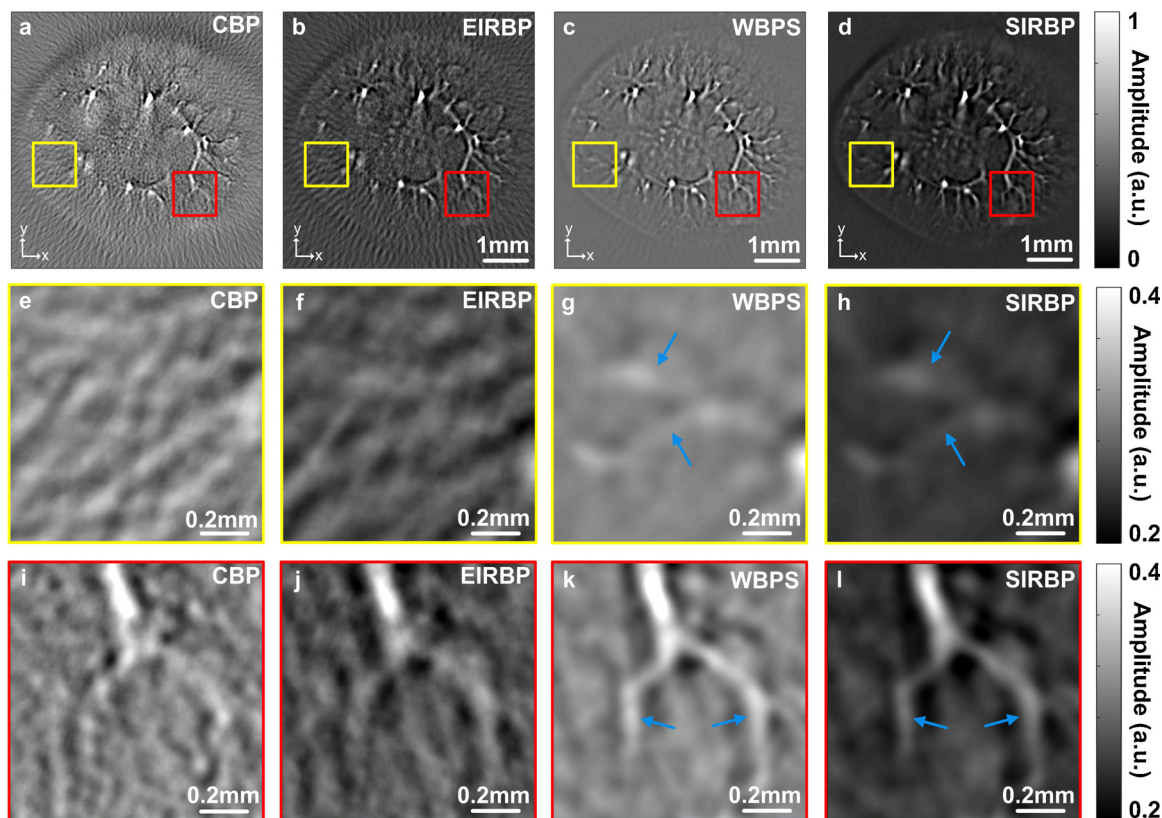
Fig. 7. (Experiment) Image reconstructions of *ex vivo* kidney of an adult mouse with (a) the CBP method, (b) the EIRBP method, (c) the WBPS method and (d) the SIRBP method. (e)-(h) are the zoom-in images of the yellow square marked in the four methods. (i)-(l) are the zoom-in images of the red square marked in the four methods. Images in the first row are shown in the same colorbar after normalization. The maximum and minimum values of the images in the second and third rows are adjusted for better observation.

are shown in the second column in Fig. 5. Both the image contrast and quality in the SIRBP result are generally improved compared to the other three results.

The reconstructed results of 100 µm-diameter microspheres (sample 2) in the ROI are presented in Fig. 6 as a further evidence. The and CBP result (Fig. 6a) WBPS result (Fig. 6c) are not able to reconstruct the spherical shape, while modeling the SIR and EIR is able to accurate reconstruct theshape of microspheres. In the zoom-in images, the SIRBP method is outperforming of suppressing the noise and homogenizing background. Overall, the shape and amplitude of the microsphere are both maintained in a high level in the SIRBP result (Fig. 6d).

Finally, the reconstructed results of the sample 3 (the *ex vivo* kidney of an adult mouse) are presented. Fig. 7a-d reveals the basic structure of this organ by the four reconstructed methods. The background noise in WBPS result (Fig. 7c) and SIRBP result (Fig. 7d) are effectively suppressed compared with the CBP result (Fig. 7a) and EIRBP result (Fig. 7b). Two particular interest regions marked by the yellow and red squares in the four methods are shown in Fig. 7e-h and Fig. 7i-l, respectively. From the zoom-in images of the yellow region in Fig. 7e-h, the CBP result (Fig. 7e) and EIRBP result (Fig. 7f) show that many tiny structures of the kidney have been buried in the background because of the strong and complex background noise, but the image contrast of EIRBP result (Fig. 7g) is better than CBP result. The shape of the tiny blood vessels is extracted and clearly recognized in both the WBPS result and SIRBP result (Fig. 7h), and the SIRBP result shows better clarity. In the red region, the extremities of the blood vessels are submerged with the background noise in the CBP result (Fig. 7i), while it can be gradually distinguished in the EIRBP result (Fig. 7j) and WBP result (Fig. 7k) from the strong background, and be observed in the SIRBP result (Fig. 7l) with highest image quality. The little branches and the boundary of vessels can be also identified in SIRBP result. These

results demonstrate that the SIRBP method offers comprehensive advantages in the image quality and fidelity.

4. Discussion

In this work, a modified back-projection reconstruction procedure fully incorporating the SIR of the employed transducer was proposed, in order to improve the image quality and fidelity of OPAM reconstructed images without additional extensive computation. The computation time of the proposed SIRBP method in a GPU framework was only about 15 times longer than the CBP method, much shorter than running time of the GPU-based model-based method considering the transducer size (approximately 2000 times longer than the CBP method [26]). The imaging performance of the SIRBP method was verified by both simulation and experiment results of phantoms and *ex vivo* biological tissue. Overall, the images obtained by the SIRBP method showed best fidelity, resolution and contrast compared with the images reconstructed by other back-projection methods.

It has been reported that only model-based method has fully considered the SIR in reconstruction process [27]. The performance of the model-based correction method in Ref [35] and the model-based method considering SIR in Ref [26] has been discussed under the scanning mode usually employed in optoacoustic tomography, shown in the Supplementary Information. Fig. S2(d) shows the SIRBP method has the greatest ability of image denoising for optoacoustic tomography. Fig. S2(b) demonstrates the shape of the absorbers can be better recovered by the model-based correction method in Ref [35] than the SIRBP method for optoacoustic tomography. However, those model-based methods are not suitable for OPAM with the large datasets because of the difficult matrix inversion and matrix construction. As the SIR is sparse at each position in the ROI, the filter matrix is sparse and

can fit into the memory of a standard computer. For the transducer with regular shape, the memory and reconstruction time can be further reduced of the symmetric ROI. Once the shape of the transducer and the ROI are confirmed, the corresponding SIR can be pre-calculated and readily employed to the three-dimensional (3D) OPAM and other arbitrary scanning geometries. In terms of the multiples from the computing time of the CBP method demonstrated in Section 2.6, the running time of the proposed SIRBP method on GPU is significantly faster than the GPU-based model-based method considering the SIR. Although the calculation time of SIRBP method has a small increase relative to CBP method, the image quality and fidelity by SIRBP method is significantly improved.

The improvement of image fidelity by the SIRBP method has been shown in the numerical simulation. Fig. 4b shows that different back-projection methods in the reconstruction results for the absorbers of different sizes exhibit different characteristics in image fidelity, respectively. The FWHMs of the absorbers in the SIRBP result are closest to their real sizes, especially for the absorbers of 60 μm-diameter and 200 μm-diameter. This indicates that the image fidelity of reconstructed image by SIRBP method is enhanced for the sample containing absorbers of different sizes. The FWHM of the 200 μm-diameter absorbers in the WBP25 result differs significantly from the real size, owing to the WBP25 method with the weighted matrix consisting of the sensitivity field of a higher frequency signal. In addition, the FWHM of the 60 μm-diameter absorbers in the WBP5 result is distinctly larger than the real size. Except the SIRBP result, the FWHMs of all absorbers in the WBP15 result and WBPS result are not much different from the actual sizes as a whole, owing to the weighted matrix consisting of the sensitivity field of a proper frequency signal and considering the influence of the SIR on the signal amplitude, respectively. Overall, the SIRBP method has a comprehensive advantage of image fidelity for the absorbers with various sizes. It's reasonable that the fidelity of the reconstructed images by SIRBP method is obviously enhanced for the full-frequency correction of the broad frequency-band optoacoustic signals.

To test the enhancement of the spatial resolution by the SIRBP method, the absorbers with diameter of 50 μm-diameter in experiment were imaged in Fig. 5. For the microspheres magnified in the second column of Fig. 5, the two adjacent microspheres indicated by red arrows suffer severe distortions in the CBP, EIRBP, and WBPS results. While they can be almost distinguished in the SIRBP result, suggesting the highest image resolution by SIRBP method, which is indeed feasible for the high-resolution OPAM imaging.

The enhancement of image contrast by use of the SIRBP method can be recognized in both simulation and experiment results. In Fig. 4a, as the size of the absorbers becomes larger, the CNR values of the SIRBP result shows an increasing trend. In the noiseless situation, the CNR value of the 60 μm-diameter absorbers in WBP25 result are higher than that in the SIRBP result, while it's opposite for the 200 μm-diameter absorbers. In the noisy situation, the CNR value of the 60 μm-diameter absorbers in SIRBP result is almost the same as that in WBP25 result. Further, the CNR values of the other absorbers in SIRBP result become highest, suggesting the stability and robustness of the SIRBP method. The experimental results of microspheres and *ex vivo* biological tissues indicates significant improvements of image contrast using SIRBP approach.

In this work, the SIRBP method models the SIR of the transducer within the BP algorithms, and can handle large datasets in OPAM and minimize the excessive time consumption. We observed that SIRBP method was providing great imaging performance over other back-projection methods which did not consider the complete SIR of the used transducer.

In conclusion, the feasibility of the SIRBP method has been verified on the 2D OPAM using a sphere-focused transducer, which is expected to be a versatile method for quickly correcting the influence of the SIR. The proposed work can further be extended to the 3D OPAM using transducers of other shapes as the computing the SIR is straightforward.

This method are now contributed to the high resolution OPAM with the large datasets, and then can be promoted to the optoacoustic tomography and other optoacoustic imaging modalities. In the future, the performance of the proposed method can be explored on the *in vivo* imaging for pre-clinical study.

Declaration of Competing Interest

We declare that we have no financial and personal relationships with other people or organizations that can inappropriately influence our work, there is no professional or other personal interest of any nature or kind in any product, service and/or company that could be construed as influencing the position presented in, or the review of, the manuscript entitled.

Acknowledgements

Appendix A. Supplementary data

Supplementary material related to this article can be found, in the online version, at doi:https://doi.org/10.1016/j.pacs.2020.100193.

References

[1] A. Taruttis, G.M. Van Dam, V. Ntziachristos, Mesoscopic and macroscopic optoacoustic imaging of cancer, Cancer Res. 75 (8) (2015) 1548–1559, https://doi.org/10.1158/0008-5472.CAN-14-2522.

[2] Y. Liu, L. Nie, X. Chen, Photoacoustic molecular imaging: from multiscale biomedical applications towards early-stage theranostics, Trends Biotechnol. 34 (5) (2016) 420–433, https://doi.org/10.1016/j.tibtech.2016.02.001.

[3] S. Jeon, J. Kim, D. Lee, J.W. Baik, C. Kim, Review on practical photoacoustic microscopy, Photoacoustics 15 (2019) 100141, , https://doi.org/10.1016/j.pacs.2019.100141.

[4] L.V. Wang, Multiscale photoacoustic microscopy and computed tomography, Nat. Photonics 3 (9) (2009) 503–509, https://doi.org/10.1038/nphoton.2009.157.

[5] T. Lu, Y. Wang, S. Zhang, J. Li, Photoacoustic mesoscopy: pushing toward the depth limit in the high-resolution optical imaging for biomedical applications and clinical potentials, Instrumentation 3 (4) (2016) 29–42, https://doi.org/10.15878/j.cnki.instrumentation.2016.04.004.

[6] M. Omar, J. Aguirre, V. Ntziachristos, Optoacoustic mesoscopy for biomedicine, Nat. Biomed. Eng. (2019), https://doi.org/10.1038/s41551-019-0377-4.

[7] M. Omar, D. Soliman, J. Gateau, V. Ntziachristos, Ultrawideband reflection-mode optoacoustic mesoscopy, Opt. Lett. 39 (13) (2014) 3911–3914, https://doi.org/10.1364/OL.39.003911.

[8] M. Omar, J. Gateau, V. Ntziachristos, Raster-scan optoacoustic mesoscopy in the 25-125MHz range, Opt. Lett. 38 (14) (2013) 2472, https://doi.org/10.1364/OL.38.002472.

[9] H.F. Zhang, K. Maslov, G. Stoica, L.V. Wang, Functional photoacoustic microscopy for high-resolution and noninvasive in vivo imaging, Nat. Biotechnol. 24 (7) (2006) 848–851, https://doi.org/10.1038/nbt1220.

[10] A. Chekkoury, A. Nunes, J. Gateau, P. Symvoulidis, A. Feuchtinger, N. Beziere, S.V. Ovsepian, A. Walch, V. Ntziachristos, High-resolution multispectral optoacoustic tomography of the vascularization and constitutive hypoxemia of cancerous tumors, Neoplasia 18 (8) (2016) 459–467, https://doi.org/10.1016/j.neo.2016.06.004.

[11] M. Schwarz, D. Soliman, M. Omar, A. Buehler, S.V. Ovsepian, J. Aguirre, V. Ntziachristos, Optoacoustic dermoscopy of the human skin: tuning excitation energy for optimal detection bandwidth with fast and deep imaging in vivo, IEEE Trans. Med. Imaging 36 (6) (2017) 1287–1296, https://doi.org/10.1109/TMI.2017.2664142.

[12] M. Schwarz, A. Buehler, J. Aguirre, V. Ntziachristos, Three-dimensional multispectral optoacoustic mesoscopy reveals melanin and blood oxygenation in human skin in vivo, J. Biophotonics 9 (1-2) (2016) 55–60, https://doi.org/10.1002/jbio.201500247.

[13] D. Razansky, V. Ntziachristos, A. Rosenthal, Acoustic inversion in optoacoustic tomography: a review, Curr. Med. Imaging Rev. 9 (4) (2013) 318–336.

[14] C. Lutzweiler, D. Razansky, Optoacoustic imaging and tomography: reconstruction approaches and outstanding challenges in image performance and quantification, Sensors 13 (6) (2013) 7345–7384, https://doi.org/10.3390/s130607345.

[15] C. Huang, K. Wang, L. Nie, L. V.Wang, M.A. Anastasio, Full-wave iterative image reconstruction in photoacoustic tomography with acoustically inhomogeneous

media, IEEE Trans. Med. Imaging 32 (6) (2013) 1097–1110, https://doi.org/10.1109/TMI.2013.2254496.

[16] Z. Jin, M.A. Anastasio, P.J.L. Riviere, L.V. Wang, Effects of different imaging models on least-squares image reconstruction accuracy in photoacoustic tomography, IEEE Trans. Med. Imaging 28 (11) (2009) 1781–1790, https://doi.org/10.1109/TMI.2009.2024082.

[17] X.L. Dean-Ben, A. Buehler, V. Ntziachristos, D. Razansky, Accurate model-based reconstruction algorithm for three-dimensional optoacoustic tomography, IEEE Trans. Med. Imaging 31 (10) (2012) 1922–1928, https://doi.org/10.1109/TMI.2012.2208471.

[18] X. Minghua, L.V. Wang, Universal back-projection algorithm for photoacoustic computed tomography, Phys. Rev. E Stat. Nonlin. Soft Matter Phys. 71 (1) (2005) 16706, https://doi.org/10.1103/PhysRevE.71.016706.

[19] J. Park, S. Jeon, J. Meng, L. Song, J.S. Lee, C. Kim, Delay-multiply-and-sum-based synthetic aperture focusing in photoacoustic microscopy, J. Biomed. Opt. 21 (3) (2016) 036010, , https://doi.org/10.1117/1.JBO.21.3.036010.

[20] A. Rosenthal, V. Ntziachristos, D. Razansky, Model-based optoacoustic inversion with arbitrary-shape detectors, Med. Phys. 38 (7) (2011) 4285–4295, https://doi.org/10.1118/1.3589141.

[21] Y. Han, L. Ding, X.L. Dean Ben, D. Razansky, J. Prakash, V. Ntziachristos, Three-dimensional optoacoustic reconstruction using fast sparse representation, Opt. Lett. 42 (5) (2017) 979–982, https://doi.org/10.1364/OL.42.000979.

[22] J. Prakash, A.S. Raju, C.B. Shaw, M. Parmanik, P.K. Yalavarthy, Basis pursuit deconvolution for improving model-based reconstructed images in photoacoustic tomography, Biomed. Opt. Express 5 (5) (2014) 1363–1377, https://doi.org/10.1364/BOE.5.001363.

[23] K. Wang, S.A. Ermilov, R. Su, H.P. Brecht, A.A. Oraevsky, M.A. Anastasio, An imaging model incorporating ultrasonic transducer properties for three-dimensional optoacoustic tomography, IEEE Trans. Med. Imaging 30 (2) (2011) 203–214, https://doi.org/10.1109/TMI.2010.2072514.

[24] M.A.A. Caballero, A. Rosenthal, A. Buehler, D. Razansky, V. Ntziachristos, Optoacoustic determination of spatio-temporal responses of ultrasound sensors, IEEE Trans. Ultrason. Ferr. 60 (6) (2013) 1234–1244, https://doi.org/10.1109/TUFFc.2013.2687.

[25] M.A.A. Caballero, Incorporating Sensor Properties in Optoacoustic Imaging, Ph.D. Dissertation, Technische Universität München, GER, 2013.

[26] L. Ding, X.L. Dean Ben, D. Razansky, Efficient three-dimensional model-based reconstruction scheme for arbitrary optoacoustic acquisition geometries, IEEE Trans. Med. Imaging 36 (9) (2017) 1858–1867, https://doi.org/10.1109/TMI.2017.2704019.

[27] M.A. Araque Caballero, J. Gateau, X.L. Dean-Ben, V. Ntziachristos, Model-based optoacoustic image reconstruction of large three-dimensional tomographic datasets acquired with an array of directional detectors, IEEE Trans. Med. Imaging 33 (2) (2014) 433–443, https://doi.org/10.1109/TMI.2013.2286546.

[28] J. Chen, R. Lin, H. Wang, J. Meng, H. Zheng, L. Song, Blind-deconvolution optical-resolution photoacoustic microscopy in vivo, Opt. Express 21 (6) (2013) 7316–7327, https://doi.org/10.1364/OE.21.007316.

[29] N.A. Rejesh, H. Pullagurla, M. Pramanik, Deconvolution-based deblurring of reconstructed images in photoacoustic/thermoacoustic tomography, J. Opt. Soc. Am. A 30 (10) (2013) 1994–2001, https://doi.org/10.1364/JOSAA.30.001994.

[30] Q. Sheng, K. Wang, T.P. Matthews, J. Xia, L. Zhu, L.V. Wang, M.A. Anastasio, A constrained variable projection reconstruction method for photoacoustic computed tomography without accurate knowledge of transducer responses, IEEE Trans. Med. Imaging 34 (12) (2015) 2443–2458, https://doi.org/10.1109/TMI.2015.2437356.

[31] K. Wang, R. Su, A.A. Oraevsky, M.A. Anastasio, Investigation of iterative image reconstruction in three-dimensional optoacoustic tomography, Phys. Med. Biol. 57 (17) (2012) 5399–5423, https://doi.org/10.1088/0031-9155/57/17/5399.

[32] D. Cai, Z. Li, Y. Li, Z. Guo, S. Chen, Photoacoustic microscopy in vivo using synthetic-aperture focusing technique combined with three-dimensional deconvolution, Opt. Express 25 (2) (2017) 1421–1434, https://doi.org/10.1364/OE.25.001421.

[33] J. Turner, H. Estrada, M. Kneipp, D. Razansky, Improved optoacoustic microscopy through three-dimensional spatial impulse response synthetic aperture focusing technique, Opt. Lett. 39 (12) (2014) 3390–3393, https://doi.org/10.1364/OL.39.003390.

[34] T. Jake, E. Héctor, K. Moritz, D. Razansky, Universal weighted synthetic aperture focusing technique (W-SAFT) for scanning optoacoustic microscopy, Optica 4 (7) (2017) 770–778, https://doi.org/10.1364/OPTICA.4.000770.

[35] M.L. Li, Y.C. Tseng, C.C. Cheng, Model-based correction of finite aperture effect in photoacoustic tomography, Opt. Express 18 (25) (2010) 26285–26292, https://doi.org/10.1364/OE.18.026285.

[36] S. Emeterio, J. Luis, Diffraction impulse response of rectangular transducers, J. Acoust. Soc. Am. 92 (2) (1992) 651–662, https://doi.org/10.1121/1.403990.

[37] M. Arditi, F.S. Foster, J.W. Hunt, Transient fields of concave annular arrays, Ultrason. Imaging 3 (1) (1981) 37–61, https://doi.org/10.1016/0161-7346(81)90081-X.

[38] J.A. Jensen, Field: A program for simulating ultrasound systems, Med. Biol. Eng. Comput. 34 (1) (1996) 351–352.

[39] B. Piwakowski, K. Sbai, A new approach to calculate the field radiated from arbitrarily structured transducer arrays, IEEE Trans. Ultrason. Ferroelectr. 46 (2) (1999) 422–440, https://doi.org/10.1109/58.753032.

[40] B.E. Treeby, Acoustic attenuation compensation in photoacoustic tomography using time-variant filtering, J. Biomed. Opt. 18 (3) (2013) 036008, , https://doi.org/10.1117/1.JBO.18.3.036008.

[41] G.F. Margrave, M.P. Lamoureux, D.C. Henley, Gabor deconvolution: estimating reflectivity by nonstationary deconvolution of seismic data, Geophysics 76 (3)

(2011) 15–30, https://doi.org/10.1190/1.3560167.

[42] J. Gateau, A. Chekkoury, V. Ntziachristos, High-resolution optoacoustic mesoscopy with a 24 MHz multidetector translate-rotate scanner, J. Biomed. Opt. 18 (10) (2013) 106005, , https://doi.org/10.1117/1.JBO.18.10.106005.

[43] B.E. Treeby, B.T. Cox, k-Wave: MATLAB toolbox for the simulation and reconstruction of photoacoustic wave fields, J. Biomed. Opt. 15 (2) (2010) 021314, , https://doi.org/10.1117/1.3360308.

Tong Lu is a PhD student in College of Precision Instrument and Optoelectronics Engineering, Tianjin University. She received her bachelor degree in Biomedical Engineering from Nanchang University. Her current research focuses on optoacoustic imaging and optoacoustic mesoscopy for phymatology researches.

Yihan Wang is currently a lecturer in the School of Life Science and Technology, Xidian University. He received his Ph.D. degree in Instrumentation Science and Technology from Tianjin University in 2019. His major research interests include the development of new functional optoacoustic/diffuse optical imaging systems and image reconstruction algorithm for pre-clinical and clinical applications.

Jiao Li is an Associate Professor in Tianjin University. She received her Ph.D. degree in Biomedical Engineering from Tianjin University in 2013, and after that she joined the School of Precision Instrument and Optoelectronics Engineering of Tianjin University. From 2015 to 2016, she was a visiting scholar at the Helmholtz Zentrum in Munich, Germany. Currently, she is working on multi-scale optoacoustic imaging with translational applications to tumor biology, and advanced molecular imaging with various functional nanomaterials and nanotechnologies for tumor theranostics.

Jaya Prakash is an Associate Professor in Indian Institute of Science. He received his Ph.D. degree from Department of Instrumentation and Applied Physics, Indian Institute of Science in 2014. Later, he moved to Munich as a Group Leader and Alexander von Humboldt Fellow at the Institute for Biological and Medical Imaging, Helmholtz Zentrum München and at the Chair for Biological Imaging, Technical University Munich, where he had worked till 2018. He works in the interface of instrumentation and computational science focused towards developing imaging systems useful for biological or medical applications.

Feng Gao is the Director of Tianjin Key Laboratory of Biomedical Detecting Techniques and Instruments, a Vice Director of Biomedical Photonics Committee of the Chinese Optical Society, and a Professor in Tianjin University. He received his Ph.D. degree in Physical Electronics from Xi'an Institute of Optics and Precision Mechanics, Chinese Academy of Sciences. His researches include biomedical spectroscopy, biomedical photonic imaging, biomedical photoelectric engineering, medical intelligence diagnosis method and instrument, and advanced radiology imaging technology.

Vasilis Ntziachristos is the Director of the Institute for Biological and Medical Imaging at the Helmholtz Zentrum in Munich, Germany, as well as a Professor of Electrical Engineering, Professor of Medicine and Chair for Biological Imaging at the Technical University Munich. He received his PhD in electrical engineering from the University of Pennsylvania, USA. His work focuses on novel innovative optical and optoacoustic imaging modalities for studying biological processes and diseases as well as the translation of these findings into the clinic.